Direct insight into the band structure of $SrNbO_3$

Chiara Bigi,[1,2,*] Pasquale Orgiani,[2,3,†] Jagoda Sławińska,[4,5] Jun Fujii,[2] John T. Irvine,[6] Silvia Picozzi,[4] Giancarlo Panaccione,[2] Ivana Vobornik,[2] Giorgio Rossi,[1,2] David Payne,[7] and Francesco Borgatti[8,‡]

[1]*Department of Physics, University of Milano, 20133 Milano, Italy*
[2]*CNR-IOM, TASC Laboratory in Area Science Park, 34139 Trieste, Italy*
[3]*CNR-SPIN, UOS Salerno, 84084 Fisciano, Italy*
[4]*Consiglio Nazionale delle Ricerche, Istituto SPIN, UOS L'Aquila, Sede di lavoro CNR-SPIN c/o Università "G. D'Annunzio," 66100 Chieti, Italy*
[5]*Department of Physics, University of North Texas, Denton, TX 76203, USA*
[6]*School of Chemistry, University of St Andrews, St Andrews, KY16 9ST, United Kingdom*
[7]*Department of Materials, Imperial College London, South Kensington, London SW7 2AZ, United Kingdom*
[8]*Consiglio Nazionale delle Ricerche – Istituto per lo Studio dei Materiali Nanostrutturati (CNR–ISMN), via P. Gobetti 101, 40129 Bologna, Italy*

(Received 27 August 2019; revised manuscript received 13 January 2020; accepted 7 February 2020; published 27 February 2020)

We present the results of a photon energy and polarization dependent angle-resolved photoemission spectroscopy (ARPES) study on high quality, epitaxial $SrNbO_3$ thin films prepared *in situ* by pulsed laser deposition (PLD). We show that the Fermi surface is composed of three bands mainly due to t_{2g} orbitals of Nb 4*d*, in analogy with the 3*d*-based perovskite systems. The bulk band dispersion for the conduction and valence states obtained by density functional theory (DFT) is generally consistent with the ARPES data. The small discrepancy in the bandwidth close to the Fermi level seems to result from the interplay of correlation effects and the presence of vacancies. The ARPES results are complemented by soft x-ray photoemission spectroscopy measurements in order to provide indications on the chemical states and the stoichiometry of the material.

DOI: 10.1103/PhysRevMaterials.4.025006

I. INTRODUCTION

The perovskites include large families of oxide compounds with the chemical formula ABO_3, *A* and *B* denoting two different cations, and a cubic lattice structure often affected by slightly distorted lower-symmetry variants [1]. For the materials hosting transition metal (TM) ions, the interplay of the electronic charge, spin and orbital degrees of freedom gives rise to a large variety of collective phenomena, such as colossal magnetoresistance, multiferroic effects, magnetocaloric behavior or superconductivity, hence bearing a huge potential impact on several technology applications [2–5]. In this framework, the behavior of perovskite oxides hosting 4*d* TM ions is expected to be quite different with respect to similar and more extensively studied 3*d* compounds. The more extended 4*d* electronic states imply increased hybridization with the surrounding oxygen ions and weaker on-site Coulomb interaction, therefore promoting a stronger metallic character and reduced electronic correlations, resulting in higher electrical conductivity. In particular, the recent interest in the early 4*d* TM perovskite $SrNbO_3$ (SNO, Nb $4d^1$ configuration) is motivated by the large charge carrier density providing metallic-like behavior as well as the visible-light photocatalytic properties [6–10]. The understanding of these properties relies mostly on theoretical descriptions of the SNO electronic structure [11–16].

In this work, we present experimental data from *in situ* angle-resolved photoemission spectroscopy (ARPES) of $SrNbO_3$ epitaxial thin films. ARPES is a direct probe of the electronic band structure and many-body interactions [17], hence we provide the first accurate experimental overview of the band structure for the $SrNbO_3$ perovskite. Previous ARPES measurements on similar compounds were performed only for the quasi-1D metallic $SrNbO_{3.41}$ phase and the ferroelectric insulator $SrNbO_{3.5}$ [18–21]. Conventional x-ray photoelectron spectroscopy for SNO is also scarcely reported [22,23], which can be due to the difficulty in fabricating high-quality thin films and the requirement of clean and ordered surfaces. However, photoemission spectroscopy has significantly contributed to the understanding of similar perovskite oxides such as $SrVO_3$ (isoelectronic d^1 occupancy) [24–27] and $SrMoO_3$ (Mo $4d^2$ configuration) [28]. We find that our results for $SrNbO_3$ from surface-sensitive ARPES and bulk band structure density functional theory (DFT) calculations are largely consistent, but a noteworthy large difference arises for the electron bands crossing the Fermi energy. In fact, the ARPES bandwidth is definitively smaller with respect to the theoretical results. Such a mass renormalisation might be related to the correlation effects and the presence of vacancies. We also performed core-level and valence states soft x-ray photoelectron spectroscopy (PES) in order to provide indications on the chemical states and the stoichiometry, and we found that the SNO thin films have a slight oxygen

*bigi@iom.cnr.it
†orgiani@iom.cnr.it
‡francesco.borgatti@cnr.it

and strontium deficiency which does not modify significantly the band structure. This demonstrates the robustness of both electronic and structural properties of this material.

II. SETUP

The $SrNbO_3$ thin films (thickness about 15 nm) were grown by pulsed laser deposition (PLD) at the APE-IOM laboratory (NFFA facility) on $DyScO_3$ (110) single-crystal substrates kept at 700 °C growth temperature while the O_2 background pressure of the PLD system was 10^{-4} mbar. The structural and morphological characterisation has been performed *in situ* through scanning tunneling microscopy (STM) and low-energy electron diffraction (LEED), and *ex situ* by x-ray diffraction (XRD) and atomic force microscopy (AFM). For these growth condition, the films exhibit compressive in-plane strain due to perfect matching with the lattice constant of the substrate, whose in-plane lattice parameter is 3.96 Å (Fig. S1 [29]), while the out-of-plane lattice parameter is 4.09 Å (Fig. S2 [29]). The temperature dependence of electrical resistivity (Fig. S5 [29]) is fully consistent with the values reported in Ref. [9] for $SrNbO_3$ films fabricated on $LaAlO_3$ insulating substrates and similar growth conditions. In both cases (our work and Ref. [9]), the larger values with respect to Ref. [6] are ascribed to the strain induced by the substrate.

ARPES ($h\nu = 30$–80 eV) and soft x-ray ($h\nu = 650$ eV) PES were performed *in-situ* at the APE beamline of the Elettra Synchrotron Radiation source [30]. For ARPES measurements, the samples were maintained at 100 K, while for soft x-ray PES the samples were kept at room temperature. The overall spectral resolution for ARPES and soft x-ray PES measurements was 60 meV and 0.5 eV, respectively.

The DFT calculations were performed with QUANTUM ESPRESSO code [31,32] using the generalized gradient approximation in the parametrization of Perdew, Burke, and Ernzerhof [33]. The electron-ion interaction was treated with the projector augmented-wave pseudopotentials [34] from the pslibrary [35], while the wave functions were expanded in a plane-wave basis of 80 Ry. We used the pseudocubic unit cell and adapted the value of lattice constant from experiment $a = 3.99$ Å. The Brillouin zone (BZ) sampling was performed following the Monkhorst-Pack scheme using a $16 \times 16 \times 16$ k-point grid, increased to $30 \times 30 \times 30$ for density of states (DOS) calculations. Further details about experimental and theoretical features are reported in Ref. [29].

III. RESULTS AND DISCUSSION

Figure 1 shows the SNO band structure along high-symmetry directions measured by ARPES and compared with the results of DFT calculations (the band structure calculated along full high-symmetry path is presented in Ref. [29]). The SNO pseudocubic lattice structure and the corresponding Brillouin zone (BZ) are shown in Figs. 1(a) and 1(b), while the experimental geometry is sketched in Fig. 1(c). The spectra acquired at normal emission with $h\nu = 40$ eV photon energy correspond to bands along the Γ-X direction [Figs. 1(d) and 1(e)], while the bands along X-M direction were detected at the photon energy $h\nu = 70$ eV [Figs. 1(f) and 1(g)]. In order to probe the orbital symmetry of the electronic states, the measurements were performed using linearly polarized radiation oriented both parallel ("π-*pol*") and perpendicular ("σ-*pol*") to the plane defined by the incidence x-ray beam direction and the analyzer axis. The band structure calculations for the Γ-X and X-M high-symmetry directions are shown in Figs. 1(h) and 1(i). The overlap of the calculations to the measurements allows for an immediate comparison.

For the bands probed along X-M direction with σ-polarized light [Fig. 1(g)], the two features located at about 5 eV binding energy and at $k = \pm 0.81$ Å^{-1} identify unambiguously the X-M high-symmetry axis, which is also confirmed by the very intense dove-shaped band located between 5 and 6 eV in case of π-polarized light. The appearance of these features along the Brillouin zone for several photon energies indicates weak dispersion. Their flatness corresponds to a high electronic mass, consistently with the indication of the DFT calculations that the band structure in the range 4–8 eV is mostly related to oxygen $2p$ orbitals. These orbitals are known to be highly localized, which manifests in an almost flat band structure. On the other hand, the intensity of the bands crossing the Fermi energy along the Γ-X direction is quite weak, thus they have been reported separately [Figs. 1(k) and 1(l)]. There are two bands that contribute to the density of states close to the Fermi level: a light parabolic one centered at Γ, and a heavy band visible along the Γ-X direction. The lack of intensity at $k = 0$ caused by π polarisation as well the strong suppression of the heavy band when the polarization is switched to σ are a typical signature of a d_{xy} orbital character, consistent with the $4d$ character. Such features have been extensively reported in ARPES studies of $3d$ based oxide perovskites [25,36,37]. We have no evidence of spectral features indicative of electron-phonon interaction neither the occurrence of a polaron regime. In the first case, the binding energy position of the related kink structure ranges between 30 and 60 meV for $SrTiO_3$ [38] and $SrVO_3$ [39], respectively, hence the energy resolution adopted in our measurements (about 50–60 meV) might have hindered its detection. On the other hand, the metallic character of the $SrNbO_3$ thin films prevents from the formation of polaronic replica of the metallic bands. This topic would probably require specific investigations through, for example, careful hole doping of the thin films in order to reduce the carrier density.

The DFT calculations for the bulk electronic structure [Figs. 1(h) and 1(i)] are similar to previous theoretical results [11,13,14,16,40] and resemble closely the band structure of the isoelectronic and isostructural $SrVO_3$ [25,26]. It can be easily noticed that all the major features of the ARPES valence bands are described correctly. In particular, the consistency with the ARPES results is also favoured by the scarce sensitivity of the $SrNbO_3$ properties to the strain induced by the substrate [40]. We emphasize that no electronic correlations were taken into account in the simulations of the band structures in Figs. 1(h) and 1(i); although we have performed additional calculations that include Hubbard corrections [41], they do not agree well with the experimental data, suggesting that more advanced techniques describing electron correlation dynamics would be necessary to fully capture the interactions in the SNO. Our calculations indicated that the bands with binding energy within 4–8 eV mainly belong to $2p$ orbitals of O, while

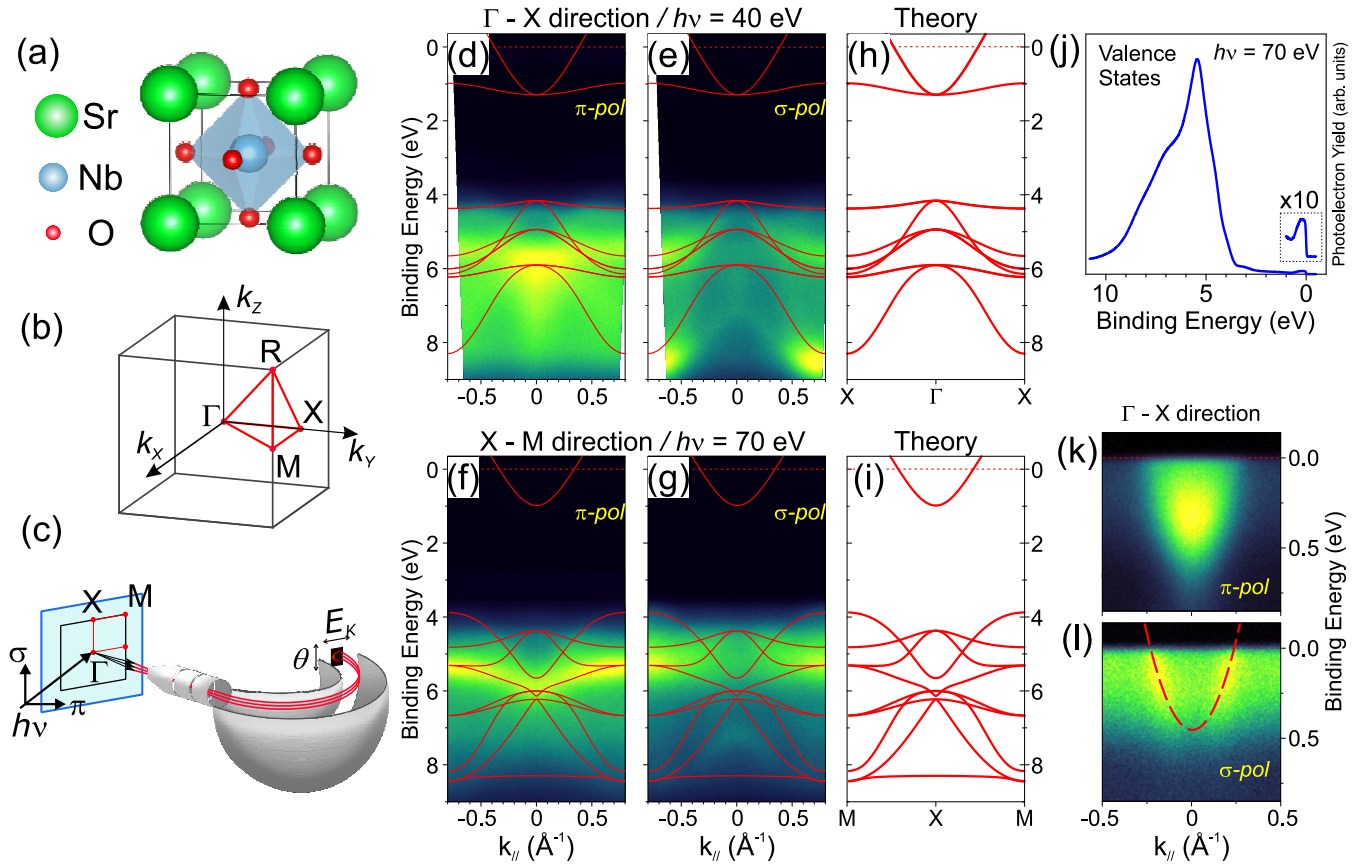

FIG. 1. [(a) and (b)] Perovskite pseudo-cubic unit cell in the direct and reciprocal space. (c) Sketch of the experimental geometry for ARPES measurements. The linear polarization π (σ) of the incident radiation is oriented in the horizontal (vertical) plane defined by the incidence direction and the analyser axis. [(d)–(g)] ARPES results as a function of light polarization of the SNO valence bands along high-symmetry directions Γ-X (h$\nu = 40$ eV) and X-M (h$\nu = 70$ eV) for both linear polarisations. These results are compared with the DFT calculations of the band structure for these specific directions. The calculations are separately shown in [(h) and (i)]; (j) integrated density of states for h$\nu = 70$ eV, with the detail of the occupied states close to the Fermi energy. The dispersion of these states along Γ-X is reported as a function of linear π and σ polarization in (k) and (l), respectively. In the latter, the parabolic fitting (dashed line) of the energy-momentum dispersion for the light conduction band crossing the Fermi energy is shown.

the Nb 4d states dominate in the Fermi edge region. The integrated density of states [Fig. 1(j)] obtained from the ARPES spectrum of Fig. 1(f) shows clearly the occupied states close to the Fermi energy, confirming the metallic state of SNO. The linear extrapolation of the valence band edge to zero intensity provides a gap energy of about 2.8 eV between the valence and the filled conduction states. This gap is much larger than the visible-light absorption energy ($\sim$1.8$-$1.9 eV) observed in ultraviolet-visible absorbance spectra [7,9], in agreement with the previous indications that this spectral feature is not related to interband transitions between those states, and that the plasmon resonance mechanism proposed in Ref. [9] in order to explain the role of SNO in the photocatalytic process should originate from the electronic excitation of the electrons in the filled conduction states.

The shape of the Fermi surface probed over the second Brillouin zone through varying the photon energy, shown in Figs. 2(a)–2(d), is consistent with the calculated bulk electronic structure Fig. 2(e) made of three bands of t_{2g} character: two spherically shaped surfaces centered at Γ point and one sheet formed by three cylinders inter-penetrating at the center of the Brillouin zone. The good agreement of the experimental results with the contour slices of the calculated Fermi surface Figs. 2(f)–2(h) indicates that photon energies of $\sim$70 and $\sim$80 eV correspond to k_z close to the Γ(002) point of the Brillouin zone. The inner potential value $V_0 = 15$ eV adopted for the experimental results was obtained through matching the measurements to the numerical calculations. As this is the first ARPES investigation on $SrNbO_3$ we cannot compare this value to previous results, however it is consistent with those reported in the literature for the isostructural and isoelectronic $SrVO_3$ perovskite oxide, ranging from $V_0 = 10$–11 eV [42] to 17–18 eV [25,27,39]. The heavy bands reach the Fermi level at $\sim$0.3 Å^{-1} along the X-M direction [see Fig. 1(b)], while the circular Fermi contour located in the center of the spectra, showing electronlike dispersion, can be assigned to the light spherical bands. The band structure close to the X-M-R plane, where only the cylindrical sheet is present, was probed with 60 eV photon energy. The finite, blurred density of state outside the circle is likely due to k_z broadening which, being related to the electron inelastic mean free path $\lambda_{IMFP} \sim 6$ Å, corresponds to few tenths of the Brillouin zone [43–45]. On the basis of the experimental results for the Fermi surface, we have estimated the number density of

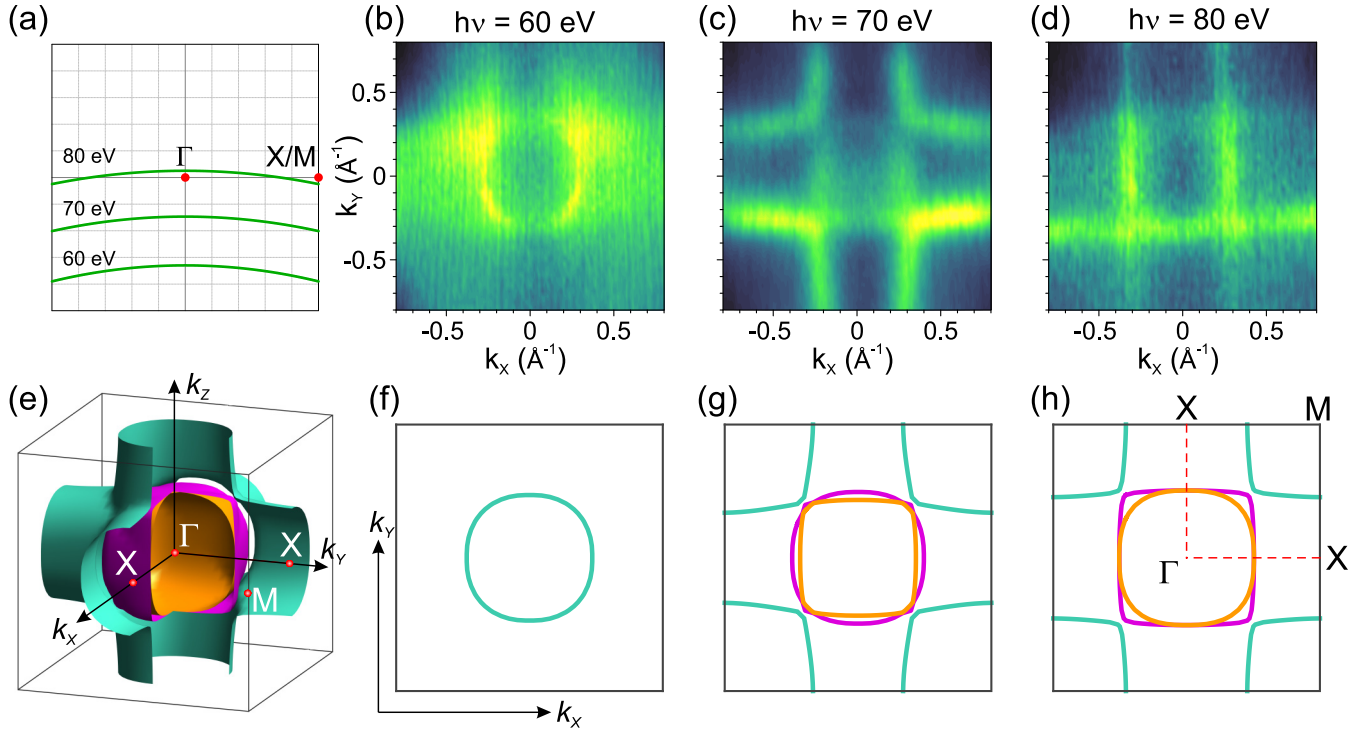

FIG. 2. Photon energy scan probing the k_z dispersion of the Fermi surface (a) Sketch of the Brillouin regions spanned by ARPES measurements. The green arcs highlight the reciprocal space positions accessible for each photon energy and mark the corresponding k_z values determined using $V_0 = 15$ eV. [(b)–(d)] experimental (k_x, k_y) slices of the Fermi surface as a function of the photon energy. (e) 3D rendering of the Fermi surface in the reciprocal space as determined by the DFT bulk calculations. [(f)–(h)] Contour plots of the Fermi surface for the same regions probed in the experiment. The shape of these curves is consistent with the experimental results.

carriers as $n \sim 10^{22}$ cm^{-3} (∼0.6 e$^-$ per unit cell volume). This value was obtained through the formula $n = V_F/(4\pi^3)$, V_F being the volume enclosed by the Fermi surface and assuming that all the three sheets forming the conduction band have an electronlike character. Such a large carrier density, fully consistent with transport results already reported in the literature [6,9,10] confirms the metallic character of SNO as expected for stoichiometry close to 1:1:3 composition. However, the parabolic fitting of the energy-momentum dispersion for the light conduction band, shown in Fig. 1(l), provides the effective electron mass $m^*_{EXPT} = 0.46m_e$ which is markedly different from the calculated value $m^*_{DFT} = 0.31m_e$. Such a difference implies a renormalisation mass factor of about 1.5 for the electrons in this band. Thus electron correlation seem to play a role in $SrNbO_3$, although the atomic radius of 4*d* transition metal ions is expected to weaken the Coulomb interaction. This result agrees with Fermi liquid behavior suggested in Ref. [6] through the study of SNO electrical conductivity. We provide here a more direct evidence of this behavior, however the assessment of the roles of Hubbard (U) and Hund (J) interactions calls for more advanced first-principles theoretical frameworks. [15,16]

Despite the overall good agreement between experimental and theoretical results, for the ARPES spectra along the Γ-*X* direction we observe some dispersion in the deeper region of the valence band centered at Γ (i.e., around 8 eV binding energy) which does not have any counterparts in the calculated bands. This difference might come from (minor) defects of the material. Given the well-known difficulty to fabricate SNO thin films with precise 1:1:3 stoichiometry, the additional states in the experimental data can be assigned to vacancies in the lattice whose presence affect the band structures. Interestingly, previous theoretical studies suggest that vacancies might introduce additional states close to the Fermi energy, reducing the energy gap [11,13]. Thus the control of these defects might be an interesting alternative to tailor the properties of SNO thin films and nanostructures for technological applications [13,14,16].

In order to elucidate this point, we have performed soft x-ray photoelectron spectroscopy of the Nb 3*d* core levels and the valence states. The results are shown in Fig. 3. Despite the moderate spectral resolution of these measurements (∼0.5 eV), the broad intensity distribution on the low binding energy side of the Nb 3*d* core-level spectrum [Fig. 3(a)] indicates the presence of multiple chemical states for the Nb ions. This result is confirmed by fitting the spectrum with a Shirley profile for the background and several doublets consisting of Voigt function line shapes with spin-orbit splitting energy 2.75 eV and statistical (3:2) branching ratio. According to Refs. [46–49], the most intense doublet [BE($3d_{5/2}$) = 207.8 eV] concerns the Nb^{5+} state, while the spectral terms at BE($3d_{5/2}$) = 206.1 and 205.0 eV correspond to the Nb^{4+} and Nb^{2+} states, respectively. The Nb^{4+} state is related to stoichiometric SNO, while the Nb^{2+} one is likely due to oxygen vacancies leaving the Nb ions in a reduced state. On the other side, the spectral contribution (S) at higher BE($3d_{5/2}$) = 209 eV can be hardly related to valence states larger than Nb^{5+} ($4d^0$). This feature could be merged into the

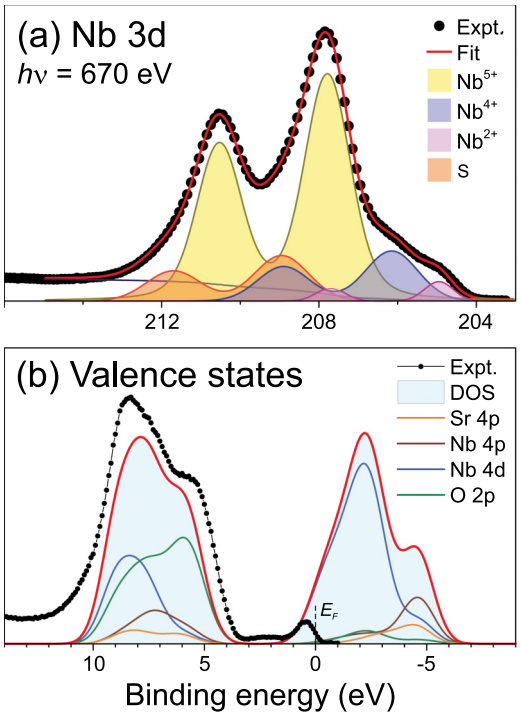

FIG. 3. Soft x-ray PES spectra measured for h$\nu = 670$ eV and normal emission geometry. (a) Nb 3d core-level spectra with the spectral contributions provided by the fitting analysis performed using coupled Voigt functions and a Shirley profile for the background. All the doublets were constrained to the same spin-orbit interval of 2.75 eV and statistical (3:2) branching ratio. The chemical states of the Nb 3d terms are indicated in the legend. (b) Experimental and theoretical density of states. The total DOS and the projected density of states were gaussian-convoluted to match the experimental spectrum. The part of calculated DOS corresponding to conduction states is shifted in energy to replicate correctly the position of the peaks in the experimental spectrum.

Nb^{5+} term through adopting an asymmetric Doniach-Sunjic profile typical of conductive materials, in agreement with the metallic behavior of this compound. In alternative, the feature might be a plasmon satellite, however the relative energy distance from the Nb 5^+ and 4^+ spectral terms (1.2 and 2.9 eV, respectively) is quite different from the plasmon energy of about 1.8 eV reported for this material [9,10]. Our results for the Nb 3d core-level spectrum resemble closely the ones achieved probing $SrMoO_3$ perovskite thin films by soft/hard x-ray PES, for which the surface was largely populated by Mo ions with chemical state Mo^{6+} ($4d^0$) while the electronic structure of the bulk was dominated by the Mo^{4+} ($4d^2$) state [28]. In our case, the depletion of the Nb valence states from 4^+ ($4d^1$) to 5^+ ($4d^0$) might have been induced by the presence of Sr vacancies in order to maintain the charge neutrality of the material, although we cannot exclude that some amount of the Nb_2O_5 secondary phase was formed at the surface. Because our soft x-ray PES results cannot distinguish unambiguously among these contributions, a clear assessment about the origin of the Nb^{5+} state and of the satellite feature will deserve further measurements able to distinguish among surface and bulk, such as angle-dependent and/or hard x-ray photoemission spectroscopy (HAXPES). However, the significant intensity near the Fermi energy in the spectrum for the density of states (DOS) shown in Fig. 3(b) confirms the metallic character of the SNO film. The spectrum is largely consistent with the theoretical DOS profile obtained summing the angular-momentum projected density of states (PDOS) for each element. The PDOS states have been weighted for the respective photoionization cross section [50] and broadened by a gaussian profile in order to match the experimental resolution. The occupied states close to E_F are mostly formed by Nb 4d states, while the O 2p states span most of the DOS in the BE region between 4 and 11 eV. These states are largely overlapped to the Nb 4p states located between 6 and 11 eV. The good agreement with the experiment suggests that the presence of Sr or O vacancies seems to affect only slightly the band structure probed through ARPES. In particular, the presence of Nb ions with empty 4d states should not affect the band structure probed around the Fermi energy. The largest effects are therefore expected for the higher BE region of the DOS dominated by Nb 4p and O 2p states, consistently with the ARPES results of Fig. 1 showing the larger deviation from the bulk electronic structure in the high BE region. Thus the band structure of these SNO epitaxial films show a substantial robustness against the presence of defects related to oxygen and/or strontium deficiency.

IV. CONCLUSIONS

In conclusion, we here report the first overview of the electronic band structure for $SrNbO_3$ through angle-resolved photoemission spectroscopy. The bulk DFT calculations well reproduce the valence band dispersions observed as a function of photon energy and polarization. In particular, the Fermi surface has been found to have a cylindrical shape which originates from t_{2g} 4d orbitals of Nb, as predicted by DFT calculations. The carrier density extracted from the volume enclosed by the Fermi surface well agrees with typical values reported for perovskites, however the bandwidth reduction and the consequent heavier effective mass shown by the ARPES spectra with respect to DFT calculations suggest the relevance of dynamical correlations and vacancies.

ACKNOWLEDGMENTS

We acknowledge G. Onida, N. Manini, G. Ruani, F. Offi and P. Gopal for stimulating discussions. This work has been performed in the framework of the Nanoscience Foundry and Fine Analysis (NFFA-MIUR Italy Progetti Internazionali) facility. This work has been supported by NOXSS PRIN (2012Z3N9R9) Project of MIUR, Italy.

[1] J. B. Goodenough and J. M. Longon, in *Magnetic and Other Properties of Oxides and Related Compounds*, edited by K.-H. Hellwege and O. Madelung, Landolt-Bornstein New Series, Group III (Springer, Berlin, 1970), Chap. 3, Vol. 4a.

[2] T. Wolfram and S. Ellialtioglu, *Electronic and Optical Properties of d-Band Perovskites* (Cambridge University Press, Cambridge, UK, 2006).

[3] S. D. Stranks and H. J. Snaith, Nat. Nanotechnol. **10**, 391 (2015).

[4] H. Y. Hwang, Y. Iwasa, M. Kawasaki, B. Keimer, N. Nagaosa, and Y. Tokura, Nat. Mater. **11**, 103 (2012).

[5] Y. Tokura and Y. Tomioka, J. Magn. Magn. Mater. **200**, 1 (1999).

[6] D. Oka, Y. Hirose, S. Nakao, T. Fukumura, and T. Hasegawa, Phys. Rev. B **92**, 205102 (2015).

[7] X. Xu, C. Randorn, P. Efstathiou, and J. T. Irvine, Nat. Mater. **11**, 595 (2012).

[8] P. Efstathiou, X. Xu, H. Ménard, and J. T. S. Irvine, Dalton Trans. **42**, 7880 (2013).

[9] D. Y. Wan, Y. L. Zhao, Y. Cai, T. C. Asmara, Z. Huang, J. Q. Chen, J. Hong, S. M. Yin, C. T. Nelson, M. R. Motapothula *et al.*, Nat. Commun. **8**, 15070 (2017).

[10] T. C. Asmara, D. Wan, Y. Zhao, M. A. Majidi, C. T. Nelson, M. C. Scott, Y. Cai, B. Yan, D. Schmidt, M. Yang *et al.*, Nat. Commun. **8**, 15271 (2017).

[11] K. Masanori, K. Mishima, and Y. Koichi, J. Photochem. Photobiol., A **375**, 175 (2019).

[12] T. Zhu, P. E. Trevisanutto, T. C. Asmara, L. Xu, Y. P. Feng, and A. Rusydi, Phys. Rev. B **98**, 235115 (2018).

[13] C. Sun and D. J. Searles, J. Phys. Chem. C **118**, 11267 (2014).

[14] S. A. Turzhevsky, D. L. Novikov, V. A. Gubanov, and A. J. Freeman, Phys. Rev. B **50**, 3200 (1994).

[15] L. de' Medici, J. Mravlje, and A. Georges, Phys. Rev. Lett. **107**, 256401 (2011).

[16] L. Vaugier, H. Jiang, and S. Biermann, Phys. Rev. B **86**, 165105 (2012).

[17] A. Damascelli, Z. Hussain, and Z.-X. Shen, Rev. Mod. Phys. **75**, 473 (2003).

[18] C. A. Kuntscher, S. Schuppler, P. Haas, B. Gorshunov, M. Dressel, M. Grioni, F. Lichtenberg, A. Herrnberger, F. Mayr, and J. Mannhart, Phys. Rev. Lett. **89**, 236403 (2002).

[19] C. A. Kuntscher, S. Schuppler, P. Haas, B. Gorshunov, M. Dressel, M. Grioni, and F. Lichtenberg, Phys. Rev. B **70**, 245123 (2004).

[20] G. Tobias and E. Canadell, J. Am. Chem. Soc. **128**, 4318 (2006).

[21] C. Chen, D. Yin, K. Inoue, F. Lichtenberg, X. Ma, Y. Ikuhara, and J. G. Bednorz, ACS nano **11**, 12519 (2017).

[22] K. Isawa, R. Itti, J. Sugiyama, N. Koshizuka, and H. Yamauchi, Phys. Rev. B **49**, 3534 (1994).

[23] T. Miruszewski, B. Kamecki, M. Łapiński, and J. Karczewski, Mater. Chem. Phys. **212**, 446 (2018).

[24] A. Sekiyama, H. Fujiwara, S. Imada, S. Suga, H. Eisaki, S. I. Uchida, K. Takegahara, H. Harima, Y. Saitoh, I. A. Nekrasov, G. Keller, D. E. Kondakov, A. V. Kozhevnikov, T. Pruschke, K. Held, D. Vollhardt, and V. I. Anisimov, Phys. Rev. Lett. **93**, 156402 (2004).

[25] M. Takizawa, M. Minohara, H. Kumigashira, D. Toyota, M. Oshima, H. Wadati, T. Yoshida, A. Fujimori, M. Lippmaa, M. Kawasaki, H. Koinuma, G. Sordi, and M. Rozenberg, Phys. Rev. B **80**, 235104 (2009).

[26] T. Yoshida, M. Kobayashi, K. Yoshimatsu, H. Kumigashira, and A. Fujimori, J. Electron Spectrosc. Relat. Phenom. **208**, 11 (2016).

[27] S. Backes, T. C. Rödel, F. Fortuna, E. Frantzeskakis, P. Le Fèvre, F. Bertran, M. Kobayashi, R. Yukawa, T. Mitsuhashi, M. Kitamura, K. Horiba, H. Kumigashira, R. Saint-Martin, A. Fouchet, B. Berini, Y. Dumont, A. J. Kim, F. Lechermann, H. O. Jeschke, M. J. Rozenberg, R. Valentí, and A. F. Santander-Syro, Phys. Rev. B **94**, 241110(R) (2016).

[28] H. Wadati, J. Mravlje, K. Yoshimatsu, H. Kumigashira, M. Oshima, T. Sugiyama, E. Ikenaga, A. Fujimori, A. Georges, A. Radetinac, K. S. Takahashi, M. Kawasaki, and Y. Tokura, Phys. Rev. B **90**, 205131 (2014).

[29] See Supplemental Material at http://link.aps.org/supplemental/10.1103/PhysRevMaterials.4.025006 for details about the fabrication of the SNO thin films, the structural and chemical characterisation, and the DFT calculations.

[30] G. Panaccione, I. Vobornik, J. Fujii, D. Krizmancic, E. Annese, L. Giovanelli, F. Maccherozzi, F. Salvador, A. De Luisa, D. Benedetti, A. Gruden, P. Bertoch, F. Polack, D. Cocco, G. Sostero, B. Diviacco, M. Hochstrasser, U. Maier, D. Pescia, C. H. Back, T. Greber, J. Osterwalder, M. Galaktionov, M. Sancrotti, and G. Rossi, Rev. Sci. Instrum. **80**, 043105 (2009).

[31] P. Giannozzi, S. Baroni, N. Bonini, M. Calandra, R. Car, C. Cavazzoni, D. Ceresoli, G. L. Chiarotti, M. Cococcioni, I. Dabo *et al.*, J. Phys.: Condens. Matter **21**, 395502 (2009).

[32] P. Giannozzi, O. Andreussi, T. Brumme, O. Bunau, M. Buongiorno Nardelli, M. Calandra, R. Car, C. Cavazzoni, D. Ceresoli, M. Cococcioni *et al.*, J. Phys.: Condens. Matter **29**, 465901 (2017).

[33] J. P. Perdew, K. Burke, and M. Ernzerhof, Phys. Rev. Lett. **77**, 3865 (1996).

[34] G. Kresse and D. Joubert, Phys. Rev. B **59**, 1758 (1999).

[35] A. D. Corso, Comput. Mater. Sci. **95**, 337 (2014).

[36] T. C. Rödel, C. Bareille, F. Fortuna, C. Baumier, F. Bertran, P. Le Fèvre, M. Gabay, O. Hijano Cubelos, M. J. Rozenberg, T. Maroutian, P. Lecoeur, and A. F. Santander-Syro, Phys. Rev. Appl. **1**, 051002 (2014).

[37] P. King, S. M. Walker, A. Tamai, A. De La Torre, T. Eknapakul, P. Buaphet, S.-K. Mo, W. Meevasana, M. Bahramy, and F. Baumberger, Nat. Commun. **5**, 3414 (2014).

[38] Z. Wang, S. M. Walker, A. Tamai, Y. Wang, Z. Ristic, F. Y. Bruno, A. de la Torre, S. Ricco, N. C. Plumb, M. Shi, P. Hlawenka, J. Sanchez-Barriga, A. Varykhalov, T. K. Kim, M. Hoesch, P. D. C. King, W. Meevasana, U. Diebold, J. Mesot, B. Moritz, T. P. Devereaux, M. Radovic, and F. Baumberger, Nat. Mater. **15**, 835 (2016).

[39] S. Aizaki, T. Yoshida, K. Yoshimatsu, M. Takizawa, M. Minohara, S. Ideta, A. Fujimori, K. Gupta, P. Mahadevan, K. Horiba, H. Kumigashira, and M. Oshima, Phys. Rev. Lett. **109**, 056401 (2012).

[40] A. Paul and T. Birol, Phys. Rev. Mater. **3**, 085001 (2019).

[41] L. A. Agapito, S. Curtarolo, and M. Buongiorno Nardelli, Phys. Rev. X **5**, 011006 (2015).

[42] T. Yoshida, K. Tanaka, H. Yagi, A. Ino, H. Eisaki, A. Fujimori, and Z.-X. Shen, Phys. Rev. Lett. **95**, 146404 (2005).

[43] H. Wadati, T. Yoshida, A. Chikamatsu, H. Kumigashira, M. Oshima, H. Eisaki, Z.-X. Shen, T. Mizokawa, and A. Fujimori, Phase Trans. **79**, 617 (2006).

[44] K. Horiba, M. Kitamura, K. Yoshimatsu, M. Minohara, E. Sakai, M. Kobayashi, A. Fujimori, and H. Kumigashira, Phys. Rev. Lett. **116**, 076401 (2016).

[45] J. Krempaský, V. N. Strocov, L. Patthey, P. R. Willmott, R. Herger, M. Falub, P. Blaha, M. Hoesch, V. Petrov, M. C. Richter *et al.*, Phys. Rev. B **77**, 165120 (2008).

[46] M. V. Kuznetsov, A. S. Razinkin, and E. V. Shalaeva, J. Struct. Chem. **50**, 514 (2009).

[47] Z. Weibin, W. Weidong, W. Xueming, C. Xinlu, Y. Dawei, S. Changle, P. Liping, W. Yuying, and B. Li, Surf. Interface Anal. **45**, 1206 (2013).

[48] T. Hadamek, A. B. Posadas, A. Dhamdhere, D. J. Smith, and A. A. Demkov, J. Appl. Phys. **119**, 095308 (2016).

[49] E. Z. Kurmaev, A. Moewes, O. G. Bureev, I. A. Nekrasov, V. M. Cherkashenko, M. A. Korotin, and D. L. Ederer, J. Alloys Compd. **347**, 213 (2002).

[50] J. Yeh and I. Lindau, At. Data Nucl. Data Tables **32**, 1 (1985).